Full paper

Stability and temporal decay of nanopatterned tribocharge on nanotextured elastomer surfaces

Myung Gi Ji [a], Qiang Li [a], Rana Biswas [a,b,c,d,*], Jaeyoun Kim [a,d,*]

[a] Department of Electrical and Computer Engineering, Iowa State University, Ames, Iowa 50011, USA
[b] Department of Physics and Astronomy, Iowa State University, Ames, Iowa 50011, USA
[c] Ames Laboratory, Iowa State University, Ames, Iowa 50011, USA
[d] Microelectronics Research Center, Iowa State University, Ames, Iowa 50011, USA

A B S T R A C T

Contact electrification of nanotextured elastomer surfaces often generates nanopatterned tribocharges that are useful for both scientific and practical purposes. For sustained utilization of the nanopatterned tribocharge, their stability and temporal behavior must be characterized and studied. It is, however, a highly challenging task as it requires long-term, repeated probing of the tribocharge at the nanoscale spatial resolution. In this work, we performed such a comprehensive experimental study of nanopatterned tribocharges on elastomer surfaces using Kelvin probe force microscopy (KPFM) and electrostatic force microscopy (EFM). Curve-fitting analysis of the KPFM results not only affirmed the temporally decaying nature of the tribocharge but also separated them into two distinct, fast and slowly decaying, components that could be attributed to two different tribocharging mechanisms. Through pre-constrained optimization of the curve-fitting parameters and comparison of the results, we could attribute the fast and slow decay components to the tribocharges generated by tangential sliding and surface-normal separation of the material interface, respectively. The analysis also enabled us to estimate time-invariant "pedestal" potentials from the KPFM results and predict the existence of long-term stable tribocharge on the nanotextured elastomer surface. We experimentally confirmed it by re-scanning the specimens 14 days after the initial measurements. The observations, analysis, and the mechano-triboelectric charging model will benefit not only the researchers of nanoscale tribocharges but also those interested in the study and applications of triboelectricity in general.

1. Introduction

Contact electrification generates electric charges on material surfaces through their contact and separation [1,2]. The phenomenon has been attributed to many different mechanisms, including electron transfer [3,4], ion transfer [5,6], or material transfer [7,8], but the resulting surface charge is commonly referred to as the tribocharge. Of recent interest is nanoscale patterning of the tribocharge [9,10] for applications in nanoscale energy harvesting [11–13], xerography [14,15], data storage [16], and virus filtration [17].

Recently, we established a new technique to generate nanopatterned tribocharges on highly deformable elastomer surfaces [18,19]. Electric charges on such soft surfaces are particularly useful for extracting energy from mechanical motion [11–13] and realization of flexible electronic devices [20]. As shown in Fig. 1, the new technique is based on

the well-known process of elastomeric replica molding. After the final demolding step (Fig. 1c), we found the surface of the elastomer strongly charged. The density of the charge turned out to depend on the level of the interfacial friction accumulated during the demolding step, revealing its triboelectric origin. By exploiting this mechano-triboelectric charging model, we could produce tribocharges in nanoscale ring and partial eclipse patterns [18,19]. The unique electric field from the ring charge distribution was subsequently utilized for nanoscale surface-texturing of photopolymer [18], opening a new avenue in the tribocharge utilization.

For sustained utilization of the tribocharge, it is imperative to characterize its temporal behavior and stability. The general consensus is that the tribocharge's density decays in time exponentially, with the timescale determined mainly by the material characteristics. In some reports, it was in the range of minutes to hours [21–26]. In others, it

spanned days to weeks [27–30]. Such discrepancies indicate that a complete characterization of the tribocharge's temporal behavior requires long-term, continuous tribocharge monitoring at one fixed sample area with the time-interval in the range of minutes at least for the first few hours. To date, reports of such a comprehensive measurement are rare [31–34].

In this paper, we describe our comprehensive study on the temporal behavior and stability of the replica molding-induced nanopatterned tribocharge. As specified above, we performed long-term, continuous measurement of the tribocharge's surface potential on one specific area of the elastomer surface using Kelvin probe force microscopy (KPFM) and electrostatic force microscopy (EFM). The measurement data was quantitatively analyzed to elucidate the tribocharge's origin. The results will provide valuable information for long-term utilization of the elastomeric tribocharge.

2. Results and analysis

2.1. Experimental setup and validation

Fig. 1 schematically depicts the technical steps of the replica molding-based contact electrification. We established it to induce various tribocharge nanopatterns on the surface of poly(dimethylsiloxane) (PDMS). Triangular lattice nanocone arrays (pitch a ~750 nm) made of poly (ethylene terephthalate) (PET) (MicroContinuum Inc.) were adopted as the master molds. We initially prepared liquid-phase PDMS (Dow Corning Sylgard 184, Dow Corning) mixed with the curing agent at 10:1 wt% ratio and desiccated the mixture for 30 mins to remove air bubbles. Then, we poured the mixture onto the master mold. Upon its complete curing, we demolded the solidified PDMS-replica from the mold. As shown in Fig. 1d, the surface of the PDMS replica exhibits a nanocup pattern.

Subsequently, we applied scanning probe microscopy techniques to map the topographical and electrical characteristics of the PDMS surface [35]. KPFM [22,36] and EFM [19,37–39] are particularly well-suited for the task since they provide high-resolution topographic and surface potential maps simultaneously. We iteratively optimized the experimental parameters of the microscope and sample preparation process to enhance the accuracy of the results [40]. Each sample was cut into a 1 cm × 1 cm square and placed in our atomic force microscope (AFM) (Multimode™, Bruker). Then we performed KPFM using a conductive Pt/Ir coated tip (SCM-PIT-V2, k = 2.8 N/m, f_o = 75 kHz, Bruker). It first scans the surface topography in the tapping mode and then lifts the tip by a fixed height to acquire the surface potential data by averaging electrostatic force from the tribocharged surface. In our work, the lift height was set to 50 nm and the scanning rate was 0.5 Hz. We carried out the KPFM measurements over the same spatial area (2 μm × 1 μm) repeatedly for 24 h.

We first attempted to check whether our experimental setup can properly reproduce our previous results [18,19] and re-affirm the mechano-triboelectric charging model [16]. Fig. 2a and b show the AFM scans performed on the PDMS-replica demolded from two different PET master molds. The nanocup's radius r and center-to-center distance a were 250 and 750 nm, respectively, which matched those of the nanocones in the master molds very closely. The depth d of the nanocups was 105 ± 6 nm (Sample A), and 45 ± 4 nm (Sample B), respectively,
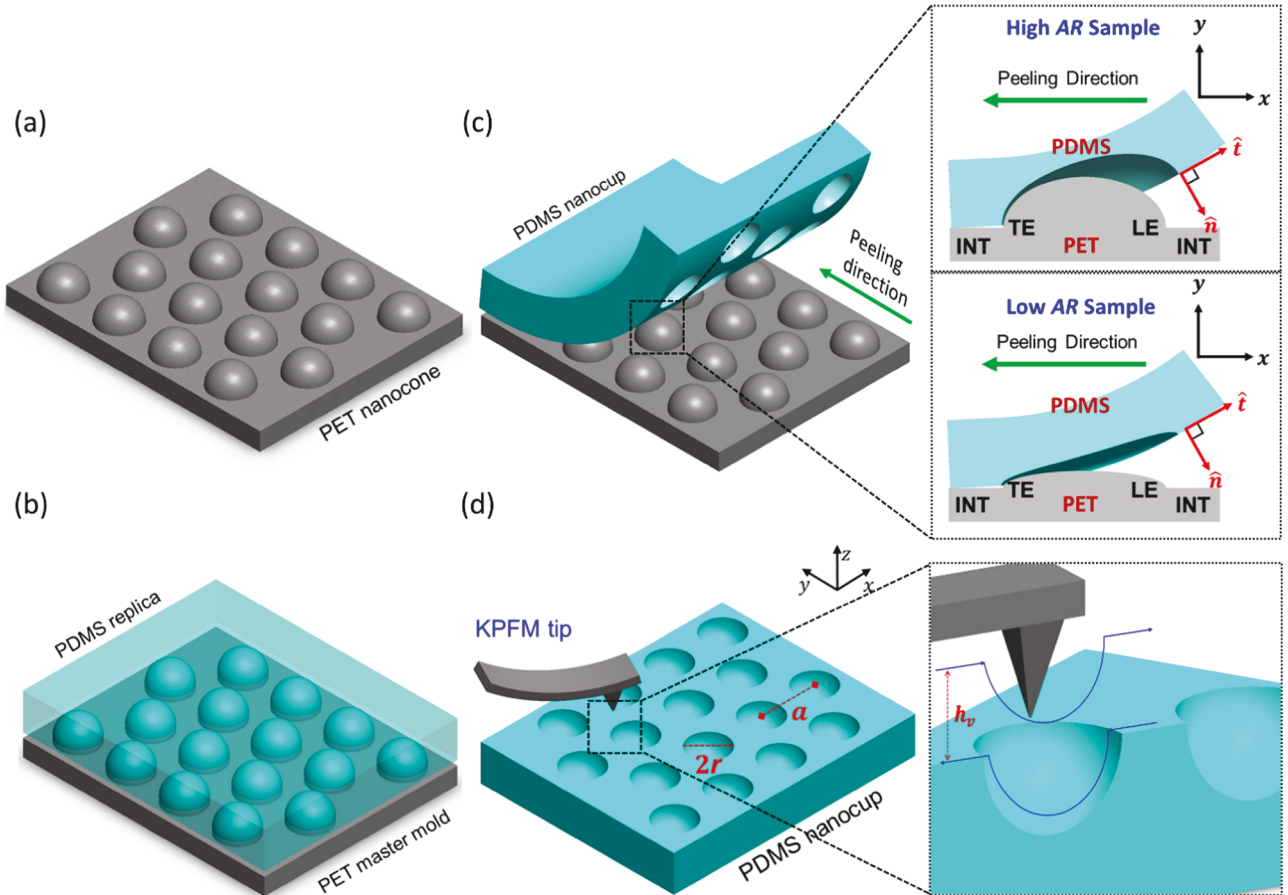

Fig. 1. (a)−(d) Replica molding-based nanopatterned tribocharge generation process: (a) A PET nanocone array master mold. (b) PDMS replication. (c) Demolding of the PDMS replica. The inset illustrates how the demolding mechanics differ for nanocones with different aspect ratios. The flat interstitial region (INT), leading edge (LE), and trailing edge (TE) are specified along the peel-off direction. (d) This process induces different levels of tribocharge on the PDMS surface to be characterized by KPFM and EFM. r, a, and h_v represent the nanocup's radius, center-to-center distance, and tip-surface separation, respectively.
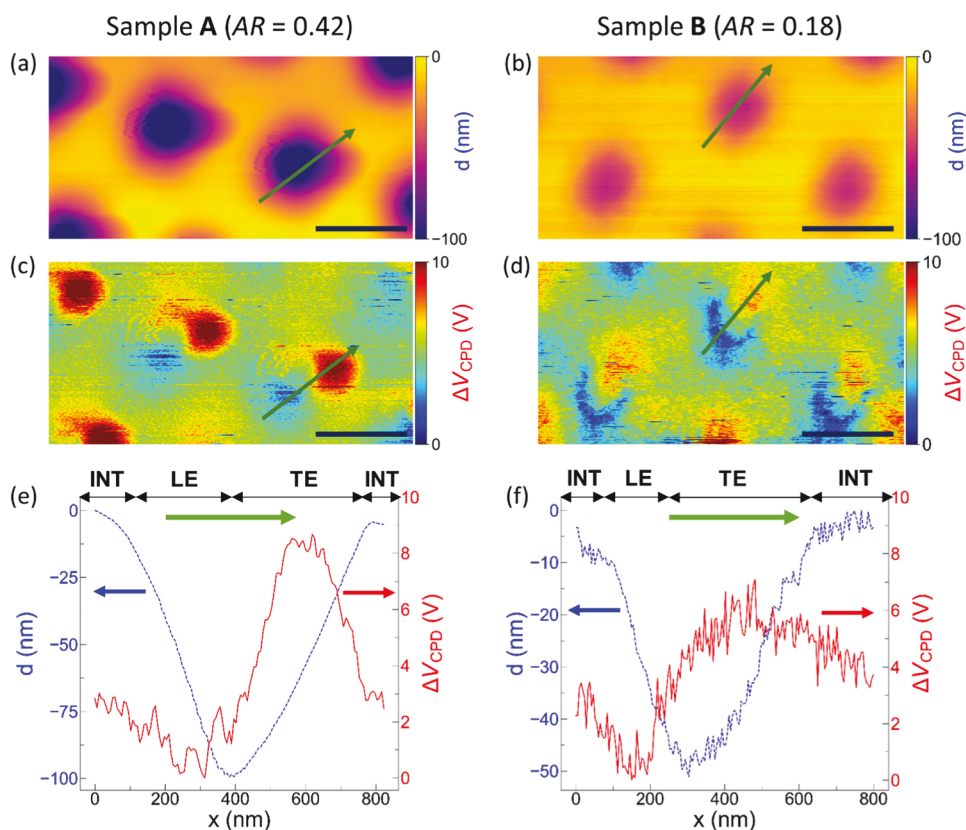
Fig. 2. (a), (b) The AFM scans of Samples A and B, with different AR, at the initial stage right after the peel-off. (c), (d) The corresponding KPFM surface potential maps of Samples A and B, respectively. (e), (f) The height (blue dotted line) and the relative surface potential ΔV_{CPD} (red solid line) profiles taken along the green arrow scan lines in (a)-(d). The black arrows in (e) and (f) specify the extents of the flat interstitial region (INT), leading edge (LE), and trailing edge (TE), respectively. The green arrows specify the peel-off directions. (Scale bars: 500 nm).

matching the heights h of the nanocones in the master molds. The corresponding aspect ratios ($AR \equiv h/r$) were 0.42 and 0.18, respectively.

Fig. 2c and d shows the KPFM scans of the surface potential (V_{CPD}) on the PDMS surface. PDMS is an insulator without a clearly defined Fermi level. Since the KPFM measurement depends critically on the tip-sample Fermi level difference, it was difficult to find the absolute values of V_{CPD}. So, we first obtained the relative contact potential difference (ΔV_{CPD}) by setting the lowest V_{CPD} level to zero. Estimation of the absolute V_{CPD} level will follow in the later part of this paper.

In both samples, the distribution pattern of ΔV_{CPD} takes the form of a partial eclipse. It agrees well with the prediction from our mechano-triboelectric charging model which related the tribocharge's distribution pattern to the surface topography of the master mold using the force arising from the demolding process as a mediating factor [18,19]. Specifically, the model states that the final tribocharge is proportional to the interfacial friction level accumulated during the peel-off action (Fig. 1c) [19]. In the current nanocone-nanocup demolding geometry, shown in the inset of Fig. 1c, the tribocharge's distribution pattern on the nanocup should exhibit its minimum and maximum in the regions corresponding to the leading and trailing edges of the nanocone, respectively, because the two edges undergo the lowest and highest levels of interfacial friction during the peel-off process.

Fig. 2e and f shows how the ΔV_{CPD} level (solid red) and the depth d (dotted blue) changed along the peel-off direction (the green arrows in Fig. 2a−d). We plotted them in superposition for facile comparison. In agreement with our argument above, the level of ΔV_{CPD} became maximized along the ascending slope of the nanocup which corresponds to the trailing edge of the nanocone. The proportionality of the tribo-electrification level on the interfacial friction also suggested that a nanocone with a higher AR would lead to a higher ΔV_{CPD} value. Comparison of the results in Fig. 2a and b reveals that it is indeed the case. For a more quantitative characterization of the tribocharge, we performed EFM on the samples and measured the charge's density and polarity. The detailed method and result can be found in Supplementary

Information.

2.2. Temporal measurement results

With the experimental setup validated, we proceeded to characterize the tribocharge's temporal behavior. To facilitate the surface potential data collection, which was planned to be a long-term, continuously repeated process, we selected a 2 μm × 1 μm area in each sample as the target area and performed KPFM scans only on it. Specifically, we scanned the target area at a regular time interval of 30 min, for 24 h. Exemplary scan results, taken at six different time points from Samples A and B, are shown in Fig. 3a and b, respectively. According to the color bars on the right, the surface potential levels of both samples decayed temporally, which indicates weakening of the tribocharge. Semi-logarithmic versions of the data plots can be found in Supplementary Information.

For a more detailed study of the tribocharge decay, we extracted temporal data from three different regions of the target area. The first two regions are the crescent- and circle-shaped regions of the partial eclipse-like pattern, *i.e.*, the blue and red regions in Fig. 2c and d, respectively. They correspond to the leading edge (LE) and the trailing edge (TE) of the PET nanocone during the peel-off process (Fig. 1c). We will refer to them as the LE and TE regions, respectively, with the corresponding surface potential denoted as V_{LE} and V_{TE}. As mentioned above, the LE and TE regions experience the lowest and the highest levels of interfacial friction during the peel-off process, respectively [18,19]. In addition, we designated the flat surface between the nanocups as the interstitial (INT) region, with the corresponding surface potential denoted as V_{INT}. The interstitial region is very important because the influence of the surface morphology, such as the size and shape of the nanocone, on the peel-off mechanics becomes minimized in it, providing an ideal location for making sample-to-sample comparisons.

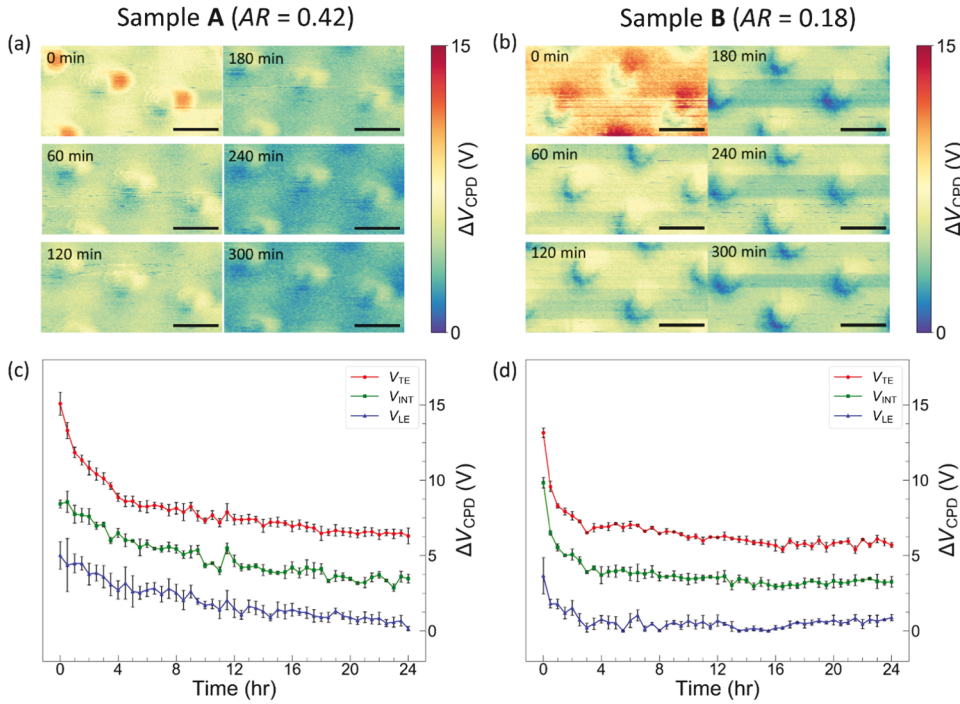We extracted ΔV_{CPD} from multiple LE, TE, and INT regions within

Fig. 3. The results of the long-term, KPFM-based surface potential measurements applied to the PDMS replicas (a) Sample A and (b) Sample B. Their patterns differ due to the difference in the AR of the nanocones in the master molds. (c)−(d) The spatially averaged maximum and minimum values of the electric potential (V_{TE}, V_{INT}, V_{LE}) as a function of time (c: Sample A, d: Sample B). The error bars represent the standard deviation obtained from each region (TE, INT, LE) within the scanned area. (Scale bars: 500 nm).

each target area and averaged the extracted ΔV_{CPD} to obtain the V_{LE}, V_{TE}, and V_{INT} data for analysis (see Methods and Materials for more details). They are plotted in Fig. 3c and d for Samples A and B, respectively. We plotted V_{LE}, V_{TE}, and V_{INT} in superposition to facilitate their comparison. In general, the plots indicate that $V_{TE} > V_{INT} > V_{LE}$, which is consistent with the shape of the ΔV_{CPD} curve in Fig. 2e and f. Some of them exhibited a clear double-decay, in which a rapid initial decay was followed by a much slower decay. In V_{LE} or V_{INT} of Sample A, however, such a double-decay was not very obvious, necessitating a more quantitative analysis.

2.3. Curve-fitting analysis

To that end, we applied curve-fitting to V_{LE}, V_{TE}, and V_{INT} using the following double-exponential function as the fitting function [31,34]:

$$V = A_f \cdot e^{-t/\tau_f} + A_s \cdot e^{-t/\tau_s} + V_{LT} \tag{1}$$

where A_f and A_s represent the amplitudes of the fast and slowly decaying exponential components, respectively, t the time, τ_f and τ_s the time constants for the fast and slow decays, respectively, and V_{LT} the long-term residual surface potential which includes the contributions from both the fast and slow decay components.

Among the three sets of surface potential data, we chose V_{INT} as the first target of the curve-fitting analysis. As mentioned above, the flat INT region is ideal for sample-to-sample comparison because the influence of the nanocone's shape and size on the peel-off mechanics becomes minimized there. One technical challenge was the strong jitter in the collected data that can make curve-fitting ambiguous by allowing many different combinations of the fitting parameters to produce similarly high correlation-squared (R^2) values. Rather than blindly pursuing the highest level of R^2, we set up one conjecture and enforced it during the curve-fitting process as a constraint. The conjecture was that the triboelectrification mechanisms responsible for the fast and slowly decaying tribocharges are common to both samples in the flat INT region. Therefore, we will be able to find identical, or very close, time constants from the V_{INT} data of both samples, i.e., $\tau_{f,A} \sim \tau_{f,B}$ and $\tau_{s,A} \sim \tau_{s,B}$. So, we tried to maximize the R^2 values in both samples simultaneously by

adjusting the values of A_f, A_s, and V_{LT}, while varying the decay time constants in conformation of the constraints.

The results are shown in the third column of Table 1. The R^2 values of the two samples' data maximized simultaneously when τ_f and τ_s were set to 0.6 and 9.5 hr, respectively. The fitting curves are plotted in Fig. 4a and b, in superposition with the data. To show the long-term decay estimation, we extended the time-axis to 48 hr. To facilitate visual comparison of the relative contributions from the fast decay, slow decay, and V_{LT} to the total result, we plotted them collectively in Fig. 4c and d. The plots show that the decay of V_{INT} in Sample A is almost single-exponential while that of Sample B is clearly double-exponential.

The fact that we could find a common set of τ_f and τ_s which is applicable to both INT regions suggests that there indeed existed two distinct triboelectric charge generation mechanisms operating in the flat INT region. The two mechanisms were common to both samples and generated two different types of triboelectric charge, each with its own decay characteristics. The computed coefficients A_f and A_s allow us to compare the strength of the two generation mechanisms in each sample. As shown in Table 1, the levels of their relative strength are very different for Samples A and B. In Sample A, A_f and A_s are 0.3 and 5.4 V, making the slow decay the dominant component. In contrast, in Sample B, they are 5.1 and 1.7 V, making the fast decay the dominant one. This difference in the dominant triboelectric generation mechanism suggests that the nanocone's size and shape still affect the triboelectric charging process even in the flat INT region.

To explain the surface morphology dependence, we extended our mechano-triboelectric charging model. As shown schematically in the enlarged Fig. 1c, during the peel-off process, the PDMS surface in the INT region becomes displaced in two directions: (i) Along the tangential $\hat{t}$-direction which rubs the PDMS surface against the PET surface, causing the interfacial friction to be accumulated, and (ii) Along the surface-normal $\hat{n}$-direction which vertically detaches the PDMS replica from the PET master mold. Our original model considered only (i). Here, we also include (ii) as a triboelectrification mechanism. The relative significance of (i) and (ii) will be determined mainly by the shape and size of the nanocones. The flat INT region surrounded by nanocones with higher AR values is less likely to undergo a significant tangential displacement as the nanocones would resist the interfacial slipping. Such

Table 1

Time constants of the fast (τ_f) and slow (τ_s) decay components, the relative strength of two charge types (A_f, A_s), and long-term residual surface potential (V_{LT}) for Samples A and B.

Sample (nanocone height, AR)	Curve-fitting parameters		V_{INT}		V_{TE}		V_{LE}	
A (110 nm, 0.42)	τ_f (hr)	τ_s (hr)	0.6	9.5	1.3	8.5	1.1	10.1
	A_f (V)	A_s (V)	0.32	5.39	4.30	4.49	0.29	4.41
	V_{LT} (V)		2.91		6.22		0.25	
	R^2		0.9581		0.9875		0.9579	
B (50 nm, 0.18)	τ_f (hr)	τ_s (hr)	0.6	9.5	0.6	10.5	0.8	3.5
	A_f (V)	A_s (V)	5.07	1.73	5.66	2.23	3.19	1.07
	V_{LT} (V)		2.95		5.46		1.13	
	R^2		0.9680		0.9679		0.8966	

a reduction in the interfacial slipping (or shear) will weaken the accumulation of the friction and, hence, lower the triboelectric charge density and the surface potential level. In contrast, the INT region surrounded by low-AR nanocones is likely to experience a higher level of interfacial slipping.

From the results in Table 1, which show the fast decay was dominant in Sample B (low AR) but almost non-existent in Sample A (high AR), we hypothesize that the fast decaying tribocharge was originated from the interfacial slipping while the slowly decaying tribocharge was generated by the surface-normal separation of the PDMS-PET interface. To verify the hypothesis, we proceeded to curve-fit V_{TE} and V_{LE}. Basically, we tried to see whether we can curve-fit the temporal data collected from the TE and LE regions with Eq. (1) using the two exponential decays obtained above, i.e., the fast decay with $\tau_f \sim$ 0.5 hr and the slow decay with $\tau_s \sim$ 10 hr and still obtain A_f and A_s values that are consistent with the model hypothesized above.

For the TE regions of Samples A and B, the best curve-fit results are shown in the 4th column of Table 1. The values of τ_f for Samples A and B were approximately 1.3 and 0.6 hr, respectively. The corresponding τ_s were approximately 8.5 and 10.5 hr, respectively. They are close to the τ_f and τ_s values obtained in the INT region (0.6 and 9.5 hr), respectively. In both cases, the R^2 values approached 0.97 and 0.99. Therefore, the TE results extend our original conjecture, that there exists a set of fast and slow decays which is common to all INT regions, into the non-flat TE regions.

The fitting curves are plotted in Fig. 5a and b in superposition with the data. Fig. 5c and d show the individual contributions of the fast decaying, slowly decaying, and long-term residual components to the overall curve-fitting results. The relative strength of the fast and slowly decaying components, which is reflected in the coefficients A_f and A_s was noticeably different in the two samples. In the TE region of Sample A (high AR), the fast decaying component, which was almost non-existent in comparison with the slowly decaying one in the INT region ($A_f/A_s \sim$ 0.059), became comparable to the slowly decaying component ($A_f/A_s \sim$ 0.95). In contrast, in Sample B (low AR), the relative strength of the fast and slowly decaying components was approximately the same in the INT and TE regions, with the A_f/A_s ratios maintained at 2.94 and 2.59, respectively.

These differences in the relative contribution levels of the fast and slow decays in the TE region are consistent with the hypothesis that the fast decaying tribocharge was originated from the interfacial slipping

while the slowly decaying tribocharge was generated by the surface-normal separation of the PDMS−PET interface. As shown in Fig. 1c, in the TE region, the peel-off action inevitably rubs the PDMS surface against the PET nanocone, increasing the interfacial friction. Indeed, the TE region of the higher-AR Sample A saw almost a factor of 16 increase in the A_f/A_s ratio in comparison to that in the INT region. On the other hand, in the lower-AR Sample B, the peel-off mechanics in the TE region is similar to that in the INT region, which explains the observation that the A_f/A_s ratios are similar in the INT and TE regions.

For the LE region, the curve-fitting results are shown in the last column of Table 1, and plotted in Fig. 6a and b. Again, we tried to enforce the τ_f and τ_s values obtained above while maximizing the R^2 values simultaneously in both samples. In Sample A, the resulting τ_f and τ_s were 1.1 and 10.1 hr, respectively. Again, they are close to the values obtained for INT and TE regions. We also found the relative strength of the fast and slow decays consistent with our model. In the high-AR Sample A, the high-AR nanocones resist the interfacial slipping and, hence, reduce the interfacial friction and the contribution of the fast decay. From the results above, we obtained a very low value of $A_f/A_s \sim$ 0.068 which is close to that obtained from the INT region ($A_f/A_s \sim$ 0.059).

In Sample B, the fitted parameters τ_f and τ_s were 0.8 and 3.5 hr, respectively. The τ_f value was consistent with the previous five results but the τ_s value was far off from the typical 9–10 hr observed in other samples or regions. We ascribe the discrepancy to the severely weaker and noisier nature of the V_{LE} data in Sample B. In fact, the highest R^2 value we could get out of it was <0.9.

Our peel-off mechanics-based interpretation still exhibited a qualitative agreement with the observations. From the low-AR case of Sample B, the mechano-triboelectric charging model predicted that the dominance of the fast decay will be maintained across the INT, LE, and TE regions, which was indeed the case. The computed A_f/A_s ratio was 2.91 which maintains the dominance of the fast decay at a level comparable to the A_f/A_s ratios obtained in the INT and TE regions (2.59 and 2.94).

To sum up, via curve-fitting of the surface potential's temporal data in the flat INT region, we identified two different, i.e., fast and slowly decaying, components. By extending our mechano-triboelectric charging model, we qualitatively attributed them to tangential slipping and the vertical separation of the material interface, respectively. Subsequently, we quantitatively showed that the extended model holds for the temporal data obtained from the LE and TE regions. To
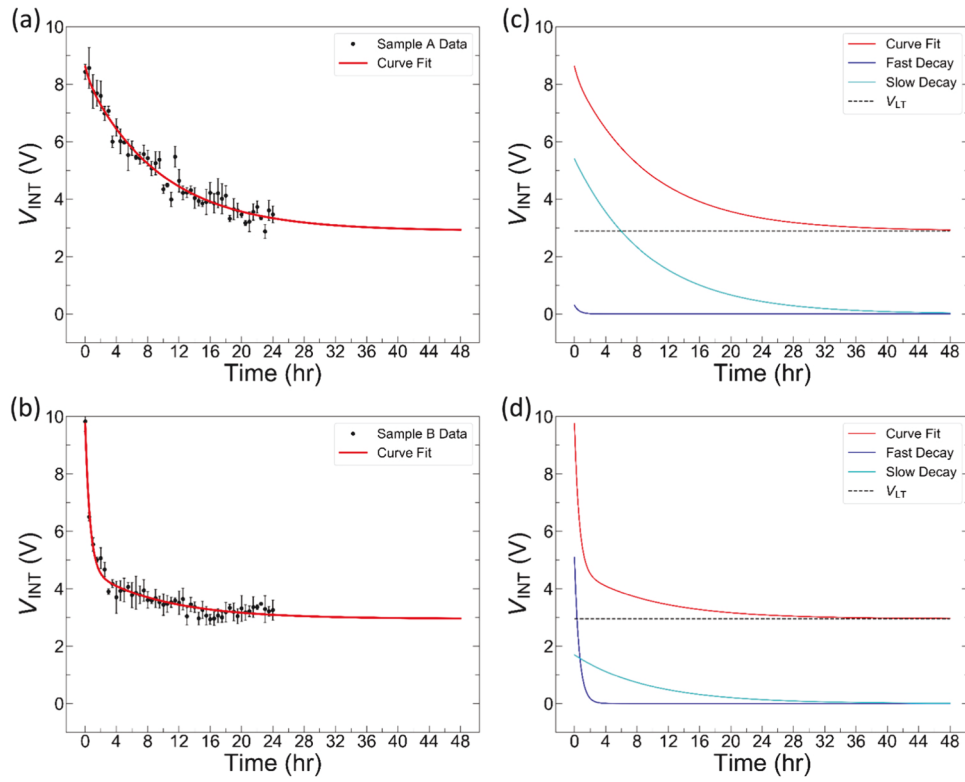
Fig. 4. The time evolution of the surface potential V_{INT} in (a) Sample A and (b) Sample B. The red solid lines represent the best fitting curves of the original data (black dots). The fitting curves are decomposed into the fast decay, slow decay, and V_{LT} in (c) for Sample A and (d) Sample B. The error bars in (a) and (b) represent the standard deviation obtained from each pattern's INT region within the scanned area.
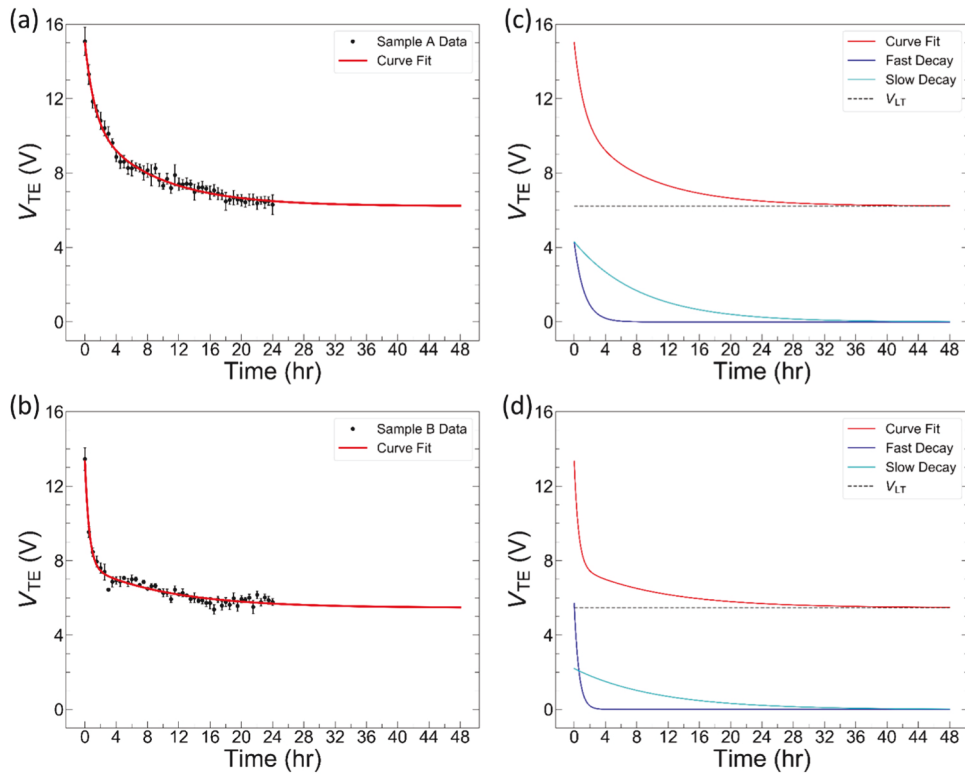

Fig. 5. The time evolution of the surface potential V_{TE} in (a) Sample A and (b) Sample B. The red solid lines represent the best fitting curves of the original data (black dots). The fitting curves are decomposed into the fast decay, slow decay, and V_{LT} in (c) for Sample A and (d) Sample B. The error bars in (a) and (b) represent the standard deviation obtained from each pattern's TE region within the scanned area.

Fig. 6. The time evolution of the surface potential V_{LE} in (a) Sample A and (b) Sample B. The red solid lines represent the best fitting curves of the original data (black dots). The fitting curves are decomposed into the fast decay, slow decay, and V_{LT} in (c) for Sample A and (d) Sample B. The error bars in (a) and (b) represent the standard deviation obtained from each pattern's LE region within the scanned area.
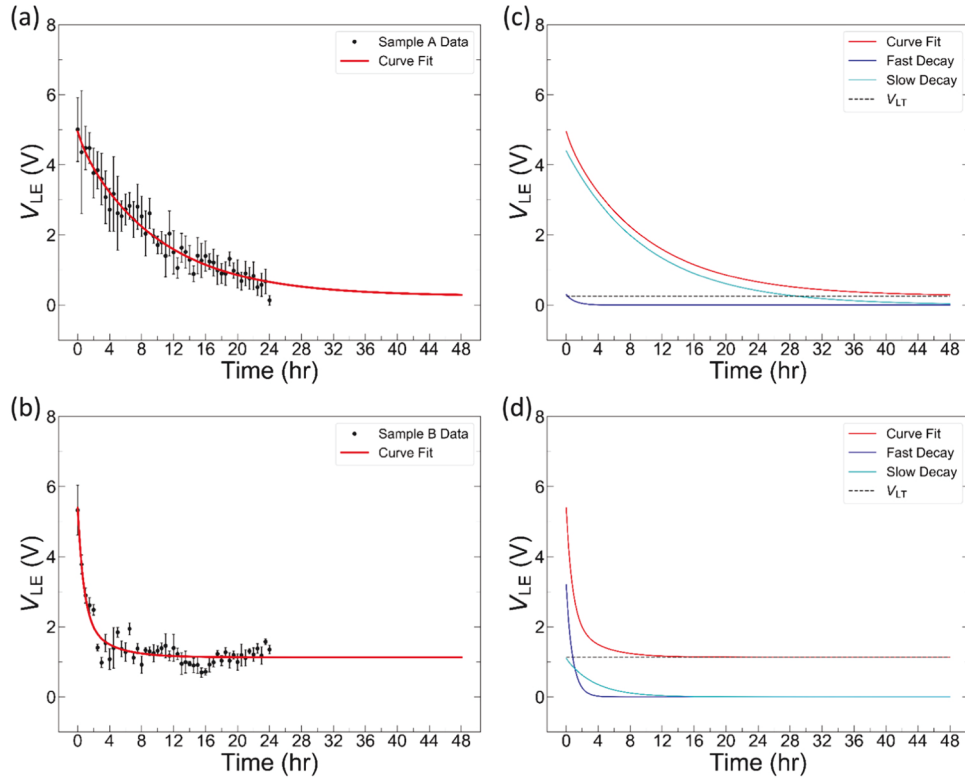
corroborate our mechano-triboelectric model, we repeated the experiments with a new set of PDMS replicas and observed a similar set of temporal behaviors and spatial dependence (Supplementary Fig. S4−S6, Supplementary Table S1).

2.4. Estimation of pedestal potential

The analysis above, however, is not complete because the absolute surface potential level V_{CPD} is not estimated yet. So far, we have only dealt with the relative potential level ΔV_{CPD} by setting the minimum point of V_{LE}, *i.e.*, the weakest potential, to zero. Axt et al. demonstrated that the stray electric field on surface affects the resolution of KPFM measurements, making it difficult to detect the absolute potential level [41]. The averaged electrostatic force of the KPFM signal can also reduce the absolute potential [42]. As will be shown in the later part of this paper, we did observe non-zero residual potential in all regions after a 24-hr period.

To find the "pedestal" potential V_P to be added commonly to V_{LE}, V_{INT}, and V_{TE} to turn them into absolute potential levels [43], we exploited the following observation: in each sample, we can find two regions in which the relative contributions of the two tribocharge generation mechanisms are almost identical. For example, in Sample A, the two tribocharge generation mechanisms in the INT and LE regions acquired the same relative strength. This can be verified by comparing the ratios of the coefficients $A_{f,INT}/A_{s,INT}$ and $A_{f,LE}/A_{s,LE}$. From Table 1, $A_{f,INT}/A_{s,INT} = 0.32/5.39 = 0.059$ and $A_{f,LE}/A_{s,LE} = 0.066$, which are very close. In Sample B, on the other hand, the two tribocharge generation mechanisms worked with the same relative strength in the INT and TE regions, with $A_{f,INT}/A_{s,INT} = 5.07/1.73 = 2.92$ very close to $A_{f,TE}/A_{s,TE} = 3.27$.

These regions form a pair with which we can estimate the overall change in the strengths of the triboelectrification mechanisms. For example, in Sample A, the overall strength of the tribocharge generation

was slightly higher in the INT region, as indicated by the ratios $A_{f,INT}/A_{f,LE} = 0.32/0.29 = 1.10$ and $A_{s,INT}/A_{s,LE} = 5.39/4.41 = 1.22$ shown in Table 2. On the average, the generation of tribocharge was strengthened by a factor of $R_{ave} \sim 1.16$ in the INT region in comparison to the LE region.

The resulting V_{LT}, however, did not increase by a similar factor. In the INT region, V_{LT} (2.91 V) was increased by a factor of more than 11 when compared with the V_{LT} value in the LE region (0.25 V) (Table 2). Such a disproportionality suggests the existence of a large pedestal potential V_P under both V_{LT} values [41,42]. Under the assumption that the V_{LT} component increases by the same factor as A_f or A_S, V_P can be computed straightforwardly by the following relation,

$$\left(V_{LT,LE} + V_P\right) \times R_{ave} = V_{LT,INT} + V_P. \tag{2}$$

Plugging in the pertinent values leads to $V_P = 16.16$ V, which is substantial in comparison to the amplitudes of the fast and slow decays.

Since we assumed that the pedestal values are proportional to the amplitudes, the total DC component, *i.e.*, the sum of V_{LT} and V_P, can be split into the fast and slow components by the ratios of $A_f/(A_f + A_s)$ and $A_s/(A_f + A_s)$ in each region, respectively. For example, in the INT region, $V_{LT,f,INT} = (V_{LT,INT} + V_P) \cdot A_f/(A_f + A_s) = 0.056 \times 19.11 = 1.07$ V and $V_{LT,s,INT} = (V_{LT,INT} + V_P) \cdot A_s/(A_f + A_s) = 0.94 \times 19.11 = 18.01$ V. Physically, the pedestal value V_P, represents the potential difference between the flat portion of the elastomeric surface and the probe, in the KPFM setup.

To check the validity of this estimation approach, we applied the same proportionality argument to the V_{TE} data of Sample A to estimate the total DC component in the TE region using the V_{INT} data. For the fast and slow decay components, the formulation leads to

$$V_{LT,f,TE} = V_{LT,f,INT} \cdot \frac{A_{f,TE}}{A_{f,INT}} \tag{3}$$

Table 2
The amplitude ratio of τ_f and τ_s in the selected region that describes the identical decaying mechanisms, the long-time residual potential V_{LT} ratio, and the estimated pedestal potential level V_P. The INT and LE region were selected for the Sample A, INT and TE regions were chosen for the Sample B.

Sample (AR)	Regions	Relative strength ratio		V_{LT} ratio	V_P (V)
Sample A (0.42)	INT/LE	$A_{f,INT}/A_{f,LE}$	$A_{s,INT}/A_{s,LE}$	2.91/ 0.25 = 11.6	16.16
		1.10	1.22		
Sample B (0.18)	INT/TE	$A_{f,INT}/A_{f,TE}$	$A_{s,INT}/A_{s,TE}$	2.95/ 5.46 = 0.54	9.59
		0.89	0.78		

$$V_{LT,s,TE} = V_{LT,s,INT} \cdot \frac{A_{s,TE}}{A_{s,INT}} \qquad (4)$$

Plugging in the pertinent values from Table 1 leads to $V_{LT,f,TE}$ = 14.35 V and $V_{LT,s,TE}$ = 15.01 V, setting the total DC component at 29.36 V. The total DC component estimated from the measurement data by adding the pedestal value to V_{LT} is 6.224 + V_P = 22.38 V, showing that the estimation based on the proportionality in qualitative agreement with the measurement data.

In the case of Sample B, the INT and TE regions form a pair. The overall strength of the tribocharge generation was higher in the TE region, as indicated by the ratios $A_{f,INT}/A_{f,TE}$= 5.07/5.66 = 0.89 and $A_{s,INT}/A_{s,TE}$ = 1.73/2.23 = 0.78. In average, the generation of the tribocharge was varied by a factor of $R_{ave} \sim$ 0.84 in the INT region in comparison to the TE region. The level of V_{LT}, however, changed at a lower rate, by a factor of 2.95/5.46 = 0.54, indicating again the existence of a pedestal level V_P. Using a relation similar to Eq. (1), we can find V_P to be 9.59 V which is also substantial in comparison to the amplitudes of the fast and slow decays.

Fig. 7 shows the estimated absolute potential level V_{CPD}, complete with the total DC component ($V_{LT} + V_P$) and the two decay components. As stated above, in the case of Sample A, the V_{INT} and V_{LE} exhibit ambiguous double decaying trends. We subsequently describe the semi-log plot to explicitly exhibit the double decaying trends for both samples with the total DC components (Supplementary Fig. S1). The total DC component may be split among the fast and slow components at a ratio determined by the relative strength of the two components. Alternatively, the total DC component can be claimed by one component exclusively. Currently, there is not enough data to reach a definite conclusion. One thing clear is that the total DC components are greater than the decay amplitudes, rendering the initial decays, fast or slow, small perturbations. All of these points to the possibility of finding long-term stable tribocharge on the PDMS surface.

2.5. Observation of long-term stable tribocharge

To explore the possibility of finding such a long-term stable tribocharge, we performed KPFM scans of Samples A and B again at the 14-day point, which is well beyond the initial 24-hr scan period or the 48-hr curve-fitting range. Fig. 8 shows the results. Note that the scanned areas were not the same target areas that we probed and reported in Figs. 2–7. Due to the nanometric length-scale of the sample features, we could not position the probe at exactly the same point twice. Therefore, the scans were performed at the closest points to the original target areas that we could locate.

Despite such a limitation, a few interesting observations were made from the results. Above all, it is clear that the surface potential on Samples A and B sustained 336 hr in uncontrolled ambience. Second, the

charge and potential distribution's details still maintained similarities to those obtained at the 24-hr point. For example, they were still in the originally observed partial eclipse-like pattern (Fig. 2), with decreased potential values. With respect to V_{LE}, the levels of V_{INT} and V_{TE} were measured to be 2.9 V and 5.4 V for Sample A and 1.3 V and 3.2 V for Sample B, respectively. Their ratios, i.e., V_{TE} / V_{INT}, were 1.87 and 2.46 for Samples A and B, respectively, which are close to the ratios obtained from the plots in Fig. 2e and f, i.e., 2.24 and 2.53 for Samples A and B.

More importantly, the newly measured V_{INT} and V_{TE} levels with respect to V_{LE} are very close to the V_{LT} level computed for each region in Table 1. For example, in Sample A, the initial values for V_{LT} in the INT and TE regions were 2.66 (= 2.91 – 0.25) and 5.97 (= 6.22 – 0.25) V, respectively, which are close to the V_{INT} and V_{TE} levels measured at the 14-day point, i.e., 3.2 V and 5.4 V, respectively. The same applies to the results obtained from Sample B. With all the similarities taken together, it is probable that the PDMS surface still maintains the $V_P + V_{LT}$ levels calculated above, retaining the long-term stable tribocharge at the corresponding densities.

For a more facile comparison of Figs. 2 and 8, their overlap plots are included as Supplementary Fig. S3. The similarities in the KPFM scan profiles indicate that the two target areas have undergone very similar peel-off processes. The consistency in the scan profiles also suggests that the spatial distribution patterns of the surface charge did not change significantly due to transport mechanisms such as diffusion [25]. This argument of the surface charge's stationarity can be further corroborated by the purity of the exponential decay curves we reported in the previous section. In general, decays involving diffusion exhibit stretched exponential curves [44,45]. Our results, while exhibiting two different time constants, remained purely exponential, minimizing the possibility that diffusion was involved in the charge's relaxation process.

3. Discussion

The findings described above can be related to the mechanisms of tribocharge generation via molecular dynamics. Classical force field-based molecular dynamics simulations [46,47] of polymer demolding from nanostructured molds have provided valuable insight into the atomistic changes occurring during the demolding process in soft lithography. They suggest that both bond-bending and bond-stretching distortions of the polymer chains occur during the demolding. In particular, the demolding process increases the radius of gyration R_g of the polymer chains, causing significant stretching of the polymer chains and a decrease in their average density [46]. Such a stretching was also found from PDMS demolding, resulting in significantly lower Young's modulus, Poisson ratio, and tensile yield stress [47].

Ab-initio electronic structure calculations [48] have shown that such stretching of polymer chains can decrease the electronic energy gaps, via changes in the highest occupied molecular (HOMO) and lowest
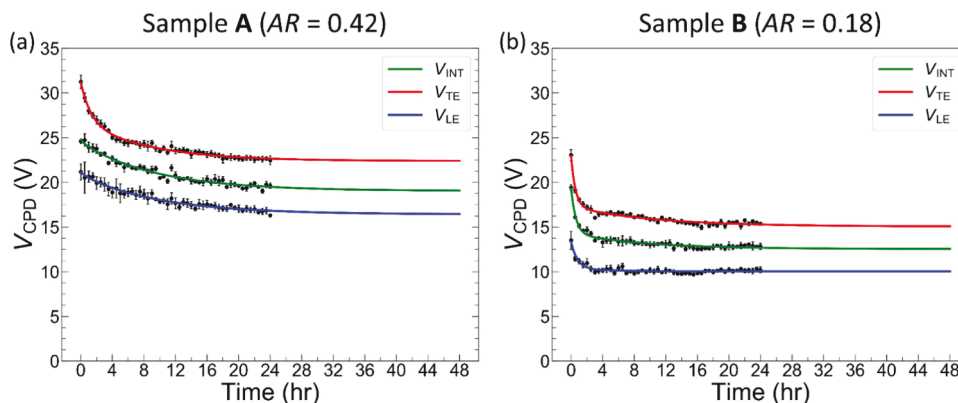
Fig. 7. The reconstructed absolute potential levels V_{CPD} of in INT, TE, and LE regions in (a) Sample A and (b) Sample B. The error bars in (a) and (b) represent the standard deviation obtained from each region (TE, INT, LE) within the scanned area.
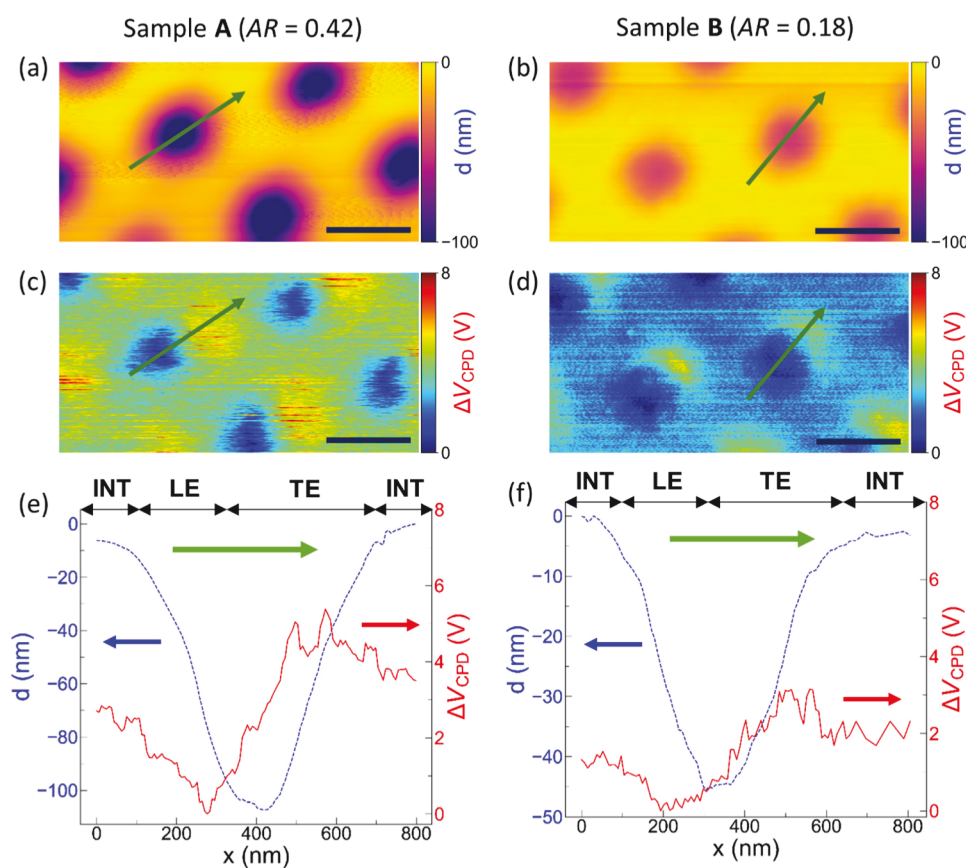

Fig. 8. The AFM and KPFM maps of Samples A and B taken at the 14-day point. (a), (b) AFM scans of Samples A and B, respectively. (c), (d) The corresponding KPFM surface potential maps of Samples A and B, respectively. (e), (f) The depth d (dotted blue) and the surface potential ΔV_{CPD} (solid red) profiles taken along the green arrow scan lines in (a)–(d). The black arrows in (e), (f) specify the INT, LE, and TE regions. The green arrows specify the peeling directions in all panels. (Scale bars: 500 nm).

unoccupied molecular (LUMO) levels, and affect the charging conditions of these nanostructures, providing important connections between the tribocharging and demolding process [49]. High-*AR* structures may induce larger distortions of the polymer chains, and consequently more significant changes in the electronic energy gaps through an increase in the HOMO and decreases in the LUMO levels, than low-*AR* ones. The upward shift of the HOMO level makes the polymer more electropositive and can lead to a stronger tribocharging. It can also lead to different temporal behaviors. We speculate that tangential sliding and surface-normal separation of the material interface may lead to predominantly bond-bending and bond-stretching distortions, respectively, with their accompanying electronic level changes producing the fast and slow components of the tribocharge temporal behavior, respectively. Further electronic structure simulations are needed to quantify this

connection.

Experimenting with heterogeneous nanocone arrays with nanocones of different *AR* values appearing alternatingly would be a decisive step to gain a deeper understanding of the tribocharging process. At the same time, the possibility that the atmospheric or surface humidity has contributed to the tribocharge generation [50,51] in conjunction with the peel-off mechanics [52] cannot be ruled out.

Recently, machine learning of our 3D KPFM data has identified the physical rules underlying contact electrification and provided a framework for reliably predicting the electric potential for more samples [53]. With the verified framework, we will be able to further improve the tribocharge generation mechanisms and the tribocharge's temporal stability, enabling its sustainable utilization and widen the application scope.

4. Conclusion

In conclusion, we have systematically studied the temporal behavior and stability of the nanoscale patterned tribocharges generated on highly deformable elastomer surfaces through the newly established replica molding technique. For data collection, we repeatedly performed short-interval KPFM scans of the same area, which turned out to be very effective in grasping both the big picture and the underlying details. The measured surface potential's temporal behavior revealed that the tribocharge underwent a double-decay in which an initial fast decay is followed by a slower one, eventually leaving only a DC component. We hypothesized that the two decays can be attributed to two distinct tribocharge groups which, in turn, can be traced to two different charging mechanisms, and performed curve-fitting analysis to verify the hypothesis. The analysis identified two exponential decay functions, with their decay time constants in the range of 0.5 hr and 10 hr, and also revealed that the two exponential decays are common to all areas and samples. By combining the curve-fitting results and the mechano-triboelectric charging model, we could attribute the fast and slowly decaying tribocharges to the tangential sliding and surface-normal separation of the material interface during the peel-off action, respectively. Furthermore, by extending the curve-fitting analysis, we estimated the DC component of the measured potential which reveals the long-term stability of the tribocharge. The analysis results indicate that both the fast and slow decays may be relatively small perturbations to the DC components. We experimentally confirmed the existence of such a long-term stable charge on the PDMS surface by measuring the surface potential levels at the 14-day point after the sample preparation. This work extends our previous mechano-triboelectric charging model by adding one more charge generation mechanism and relating it to the tribocharge's temporal behavior. Both the model and the analysis method can be utilized to analyze and predict the spatial and temporal behaviors of the tribocharges on elastomer surfaces, facilitating their future utilizations for energy harvesting, flexible electronics and medical applications.

5. Methods and materials

5.1. Fabrication of the tribocharged PDMS nanocup arrays

To fabricate the tribocharged PDMS nanocup arrays, we initially prepared two different types of PET molds with a 750 nm-pitch triangular array of nanocones (500 nm in base diameter, 110 nm (Sample A) and 50 nm (Sample B) in height, MicroContinuum Inc.). We proceeded to prepare liquid phase PDMS (Sylgard 184, Dow Corning) mixed with curing agent 10:1 wt% and desiccated the mixture for 30 min to remove air bubbles. Then, we poured the PDMS mixture onto the PET master molds. The PET master molds with the liquid-phase PDMS was placed on the hot plate (65 °C) over 24 h. Upon its complete solidification, we peeled the PDMS off from the master molds obtaining a matching nanocup array. The depth d of the nanocup arrays was varied to be 105 ± 6 nm (Sample A), and 45 ± 4 nm (Sample B).

5.2. Tribocharge characterization via AFM/KPFM

Each sample was cut into a 1 cm × 1 cm square and placed in atomic force microscope (AFM) (Multimode, Bruker) to characterize the surface morphology. Then we carried out the KPFM using a conductive Pt/Ir coated tip (SCM-PIT-V2, $k = 2.8$ N/m, $f_0 = 75$ kHz, Bruker) for 24 h. The lift height was set to 50 nm and the scanning rate was 0.5 Hz over the same spatial area (2 μm × 1 μm) for 24 h. The time interval was set to 30 mins to provide sufficient data points.

5.3. Extraction of regional surface potential data

The V_{LE}, V_{TE}, and V_{INT} values for further analysis were obtained as follows. We first separated the target area (2 μm × 1 μm) into the crescent-shaped and circle-shaped regions (shown in Fig. 2c and d) and marked them as the LE and TE regions. The rest of the target area was marked as the INT region. Then, we collected the measured surface potential from 3 LE and TE regions. From each LE and TE region, we collected 4 data sets, making the total data count 12. From the INT region, we also collected 4 data sets. Then, we obtained their averages and standard deviations that are plotted in Fig. 3. The spatial interval for the KPFM probe's scanning operation was 5 nm in both horizontal and vertical directions. Since the LE and TE regions took the shape of circles and crescents with >100 nm extents, we could safely set multiple data points near the center of the regions and record the values.

Notes

The authors declare no competing financial interest.

CRediT authorship contribution statement

Myung Gi Ji: Experimental set up, Formal analysis, Investigation, Writing - original draft, Visualization, Data analysis. **Qiang Li**: Methodology, Investigation, Experimental set up, Writing - original draft. **Rana Biswas**: Idea Conceptualization, Supervision, Project administration, Funding acquisition, Investigation, Formal Analysis, Writing - original draft, Writing - review & editing. **Jaeyoun Kim**: Idea Conceptualization, Supervision, Project administration, Funding acquisition, Investigation, Formal analysis, Writing - original draft, Writing - review & editing.

Declaration of Competing Interest

The authors declare that they have no known competing financial interests or personal relationships that could have appeared to influence the work reported in this paper.

Appendix A. Supporting information

Supplementary data associated with this article can be found in the online version at doi:10.1016/j.nanoen.2020.105441.

References

[1] L.S. McCarty, A. Winkleman, G.M. Whitesides, Ionic electrets: electrostatic charging of surfaces by transferring mobile ions upon contact, J. Am. Chem. Soc. 129 (2007) 4075–4088, https://doi.org/10.1021/ja067301e.

[2] J. Lowell, A.C. Rose-Innes, Contact electrification, Adv. Phys. 29 (1980) 947–1023, https://doi.org/10.1080/00018738000101466.

[3] D.J. Lacks, T. Shinbrot, Long-standing and unresolved issues in triboelectric charging, Nat. Rev. Chem. 3 (2019) 465–476, https://doi.org/10.1038/s41570-019-0115-1.

[4] H. Zou, Y. Zhang, L. Guo, P. Wang, X. He, G. Dai, H. Zheng, C. Chen, A.C. Wang, C. Xu, Z.L. Wang, Quantifying the triboelectric series, Nat. Commun. 10 (2019) 1–9, https://doi.org/10.1038/s41467-019-09461-x.

[5] N. Knorr, Squeezing out hydrated protons: low-frictional-energy triboelectric insulator charging on a microscopic scale, AIP Adv. 1 (2011), 022119, https://doi.org/10.1063/1.3592522.

[6] R. Fu, X. Shen, D.J. Lacks, First-principles study of the charge distributions in water confined between dissimilar surfaces and implications in regard to contact electrification, J. Phys. Chem. C 121 (2017) 12345–12349, https://doi.org/10.1021/acs.jpcc.7b04044.

[7] R.K. Pandey, H. Kakehashi, H. Nakanishi, S. Soh, Correlating material transfer and charge transfer in contact electrification, J. Phys. Chem. C 122 (2018) 16154–16160, https://doi.org/10.1021/acs.jpcc.8b04357.

[8] H.T. Baytekin, B. Baytekin, J.T. Incorvati, B.A. Grzybowski, Material transfer and polarity reversal in contact charging, Angew. Chem. Int. Ed. 51 (2012) 4843–4847, https://doi.org/10.1002/anie.201200057.

[9] H.O. Jacobs, G.M. Whitesides, Submicrometer patterning of charge in thin-film electrets, Science 291 (2001) 1763–1766, https://doi.org/10.1126/science.1057061.

[10] F.R. Fan, L. Lin, G. Zhu, W. Wu, R. Zhang, Z.L. Wang, Transparent triboelectric nanogenerators and self-powered pressure sensors based on micropatterned plastic films, Nano Lett. 12 (2012) 3109–3114, https://doi.org/10.1021/nl300988z.

[11] K.Y. Lee, J. Chun, J.H. Lee, K.N. Kim, N.R. Kang, J.Y. Kim, M.H. Kim, K.S. Shin, M. K. Gupta, J.M. Baik, S.W. Kim, Hydrophobic sponge structure-based triboelectric nanogenerator, Adv. Mater. 26 (2014) 5037–5042, https://doi.org/10.1002/adma.201401184.

[12] S.S. Kwak, H.J. Yoon, S.W. Kim, Textile-based triboelectric nanogenerators for self-powered wearable electronics, Adv. Funct. Mater. 29 (2019) 1–26, https://doi.org/10.1002/adfm.201804533.

[13] Y. Bai, L. Xu, S. Lin, J. Luo, H. Qin, K. Han, Z.L. Wang, Charge pumping strategy for rotation and sliding type triboelectric nanogenerators, Adv. Energy Mater. 10 (2020) 1–9, https://doi.org/10.1002/aenm.202000605.

[14] H.O. Jacobs, S.A. Campbell, M.G. Steward, Approaching nanoxerography: the use of electrostatic forces to position nanoparticles with 100 nm scale resolution, Adv. Mater. 14 (2002) 1553–1557, https://doi.org/10.1002/1521-4095(20021104)14:21<1553::AID-ADMA1553>3.0.CO;2-9.

[15] E. Palleau, L. Ressier, Combinatorial particle patterning by nanoxerography, Adv. Funct. Mater. 28 (2018) 4–7, https://doi.org/10.1002/adfm.201801075.

[16] S.Y. Kuang, G. Zhu, Z.L. Wang, Triboelectrification-enabled self-powered data storage, Adv. Sci. 5 (2018) 1–8, https://doi.org/10.1002/advs.201700658.

[17] S.B. Martin, E.S. Moyer, Electrostatic respirator filter media: filter efficiency and most penetrating particle size effects, Appl. Occup. Environ. Hyg. 15 (2000) 609–617, https://doi.org/10.1080/10473220050075617.

[18] Q. Li, A. Peer, I.H. Cho, R. Biswas, J. Kim, Replica molding-based nanopatterning of tribocharge on elastomer with application to electrohydrodynamic nanolithography, Nat. Commun. 9 (2018), https://doi.org/10.1038/s41467-018-03319-4.

[19] Q. Li, I.H. Cho, R. Biswas, J. Kim, Nanoscale modulation of friction and triboelectrification via surface nanotexturing, Nano Lett. 19 (2019) 850–856, https://doi.org/10.1021/acs.nanolett.8b04038.

[20] J. Wang, S. Qian, J. Yu, Q. Zhang, Z. Yuan, S. Sang, X. Zhou, L. Sun, Flexible and wearable PDMS-based triboelectric nanogenerator for self-powered tactile sensing, Nanomaterials 9 (2019), https://doi.org/10.3390/nano9091304.

[21] J. Yin, B. Nysten, Contact electrification and charge decay on polyester fibres: a KPFM study, J. Electro 96 (2018) 16–22, https://doi.org/10.1016/j.elstat.2018.09.002.

[22] X. Qian, Z. Lin, L. Guan, Q. Li, Y. Wang, M. Zhang, M. Dong, In situ probing the relaxation properties of ultrathin polystyrene films by using electric force microscopy, Nanoscale Res. Lett. 12 (2017) 257, https://doi.org/10.1186/s11671-017-2019-7.

[23] Z.H. Lin, D. Gao, L. Guan, M. Zhang, X. Zhu, Y. Yang, X. Qiu, J.P. Zhang, Charge-pattern indicated relaxation dynamics and glass transition of polymer thin films studied by atomic force microscopy, J. Phys. Chem. C 120 (2016) 12157–12162, https://doi.org/10.1021/acs.jpcc.6b04656.

[24] Y.S. Zhou, Y. Liu, G. Zhu, Z.H. Lin, C. Pan, Q. Jing, Z.L. Wang, In situ quantitative study of nanoscale triboelectrification and patterning, Nano Lett. 13 (2013) 2771–2776, https://doi.org/10.1021/nl401006x.

[25] H.T. Baytekin, A.Z. Patashinski, M. Branicki, B. Baytekin, S. Soh, B.A. Grzybowski, The mosaic of surface charge in contact electrification, Science 333 (2011) 308–312, https://doi.org/10.1126/science.1201512.

[26] J. Zhang, F.J.M. Rogers, N. Darwish, V.R. Gonçales, Y.B. Vogel, F. Wang, J. J. Gooding, M.C.R. Peiris, G. Jia, J.P. Veder, M.L. Coote, S. Ciampi, Electrochemistry on tribocharged polymers is governed by the stability of surface charges rather than charging magnitude, J. Am. Chem. Soc. 141 (2019) 5863–5870, https://doi.org/10.1021/jacs.9b00297.

[27] X. Ma, Z. Xie, Z. Liu, X. Liu, T. Cao, Z. Zheng, Polymer brush electrets, Adv. Funct. Mater. 23 (2013) 3239–3246, https://doi.org/10.1002/adfm.201203181.

[28] T.A. de L. Burgo, C.A. Rezende, S. Bertazzo, A. Galembeck, F. Galembeck, Electric potential decay on polyethylene: role of atmospheric water on electric charge build-up and dissipation, J. Electro 69 (2011) 401–409, https://doi.org/10.1016/j.elstat.2011.05.005.

[29] L. Ressier, V. Le Nader, Electrostatic nanopatterning of PMMA by AFM charge writing for directed nano-assembly, Nanotechnology 19 (2008), 135301, https://doi.org/10.1088/0957-4484/19/13/135301.

[30] C. Xu, Y. Zi, A.C. Wang, H. Zou, Y. Dai, X. He, P. Wang, Y.C. Wang, P. Feng, D. Li, Z. L. Wang, On the electron-transfer mechanism in the contact-electrification effect, Adv. Mater. 30 (2018) 1–9, https://doi.org/10.1002/adma.201706790.

[31] E.A. Baum, T.J. Lewis, R. Toomer, Decay of electrical charge on polyethylene films, J. Phys. D Appl. Phys. 10 (1977) 487–497, https://doi.org/10.1088/0022-3727/10/4/013.

[32] J.T. Jones, P.M. Bridger, O.J. Marsh, T.C. McGill, Charge storage in $CeO_2/Si/CeO_2/Si(111)$ structures by electrostatic force microscopy, Appl. Phys. Lett. 75 (1999) 1326–1328, https://doi.org/10.1063/1.124682.

[33] N. Knorr, S. Rosselli, G. Nelles, Surface-potential decay of biased-probe contact-charged amorphous polymer films, J. Appl. Phys. 107 (2010), 054106, https://doi.org/10.1063/1.3309763.

[34] Y. Zhuang, G. Chen, P.H. Chappell, M. Rotaru, Surface potential decay: effect of different corona charging times. Conference on Electrical Insulation and Dielectric Phenomena, CEIDP (2012) 620–623, https://doi.org/10.1109/CEIDP.2012.6378857.

[35] B.D. Terris, J.E. Stern, D. Rugar, H.J. Mamin, Localized charge force microscopy, J. Vac. Sci. Technol. A Vac. Surf. Film. 8 (1990) 374–377, https://doi.org/10.1116/1.576399.

[36] J. Wang, J.J. Xu, X. Wang, H.T. Cao, L.H. Xie, M.D. Yi, W. Huang, Excellent charge-storage properties of polystyrene/SFXs electret films by repeated contact with an AFM probe, Phys. Status Solidi Basic Res. 255 (2018) 1–4, https://doi.org/10.1002/pssb.201700611.

[37] D. El Khoury, R. Arinero, J.C. Laurentie, J. Castellon, Nanoscale surface charge detection in epoxy resin materials using electrostatic force spectroscopy, AIP Adv. 6 (2016), 035318, https://doi.org/10.1063/1.4944953.

[38] J. Deschler, J. Seiler, J. Kindersberger, Detection of charges at the interphase of polymeric nanocomposites, IEEE Trans. Dielectr. Electr. Insul. 24 (2017) 1027–1037, https://doi.org/10.1109/TDEI.2017.006387.

[39] Y.J. Kim, C.H. Yang, Electret formation in transition metal oxides by electrochemical amorphization, NPG Asia Mater. 12 (2020) 1–9, https://doi.org/10.1038/s41427-019-0187-x.

[40] A. Liscio, V. Palermo, K. Müllen, P. Samorì, Tip − sample interactions in Kelvin probe force microscopy: Quantitative measurement of the local surface potential, J. Phys. Chem. C 112 (2008) 17368–17377, https://doi.org/10.1021/jp806657k.

[41] A. Axt, I.M. Hermes, V.W. Bergmann, N. Tausendpfund, S.A.L. Weber, Know your full potential: quantitative Kelvin probe force microscopy on nanoscale electrical devices, Beilstein J. Nanotechnol. 9 (2018) 1809–1919, https://doi.org/10.3762/bjnano.9.172.

[42] D. Ziegler, A. Stemmer, Force gradient sensitive detection in lift-mode Kelvin probe force microscopy, Nanotechnology 22 (2011), 075501, https://doi.org/10.1088/0957-4484/22/7/075501.

[43] S. Lin, L. Xu, A. Chi Wang, Z.L. Wang, Quantifying electron-transfer in liquid-solid contact electrification and the formation of electric double-layer, Nat. Commun. 11 (2020) 1–8, https://doi.org/10.1038/s41467-019-14278-9.

[44] J. Kakalios, R.A. Street, W.B. Jackson, Stretched-exponential relaxation arising from dispersive diffusion of hydrogen in amorphous silicon, Phys. Rev. Lett. 59 (1987) 1037–1040, https://doi.org/10.1103/PhysRevLett.59.1037.

[45] J.H. Kim, B.K. Yun, J.H. Jung, J.Y. Park, Enhanced triboelectrification of the polydimethylsiloxane surface by ultraviolet irradiation, Appl. Phys. Lett. 108 (2016), 133901, https://doi.org/10.1063/1.4945052.

[46] C. Weng, D. Yang, M. Zhou, Molecular dynamics simulations on the demolding process for nanostructures with different aspect ratios in injection molding, Micromachines 10 (2019) 636, https://doi.org/10.3390/mi10100636.

[47] A.H. Abdul Manap, S.S. Md Izah, K. Mohamed, Molecular dynamics study of poly (dimethylsiloxane) nanostructure distortion in a soft lithography demolding process, ACS Omega 4 (2019) 20257–20264, https://doi.org/10.1021/acsomega.9b02547.

[48] J.C. Roldao, A. Batagin-Neto, F.C. Lavarda, F. Sato, Effects of mechanical stretching on the properties of conjugated polymers: case study for MEH-PPV and P3HT oligomers, J. Polym. Sci. Part B Polym. Phys. 56 (2018) 1413–1426, https://doi.org/10.1002/polb.24731.

[49] J. Nie, Z. Ren, L. Xu, S. Lin, F. Zhan, X. Chen, Z.L. Wang, Probing contact-electrification-induced electron and ion transfers at a liquid–solid interface, Adv. Mater. 32 (2020) 1–11, https://doi.org/10.1002/adma.201905696.

[50] H.T. Baytekin, B. Baytekin, S. Soh, B.A. Grzybowski, Is water necessary for contact electrification? Angew. Chem. Int. Ed. 50 (2011) 6766–6770, https://doi.org/10.1002/anie.201008051.

[51] L.S. McCarty, G.M. Whitesides, Electrostatic charging due to separation of ions at interfaces: contact electrification of ionic electrets, Angew. Chem. Int. Ed. 47 (2008) 2188–2207, https://doi.org/10.1002/anie.200701812.

[52] L. Santos, Y. Campo, D. da Silva, T. Burgo, F. Galembeck, Rubber surface change and static charging under periodic stress, Colloids Interfaces 2 (2018) 55, https://doi.org/10.3390/colloids2040055.

[53] I.H. Cho, Q. Li, R. Biswas, J. Kim, A framework for glass-box physics rule learner and its application to nano-scale phenomena, Commun. Phys. 3 (2020) 1–9, https://doi.org/10.1038/s42005-020-0339-x.

Myung Gi Ji received his B.S. degree and M.S. degree in Electrical and Electronic Engineering from Chung-Ang University (Seoul, South Korea) in 2015 and 2017, respectively. Currently, he is a Ph.D. candidate in Electrical Engineering under supervision of Prof. Jaeyoun (Jay) Kim at Iowa State University in USA. His research interests mainly focus on nanotextured triboelectrification on soft materials.

Rana Biswas received his Ph.D. in Physics from Cornell University in 1984. From 1984–1986, he was a postdoctoral member of Technical Staff at AT&T Bell Laboratories, Murray Hill, NJ, after which he moved to Iowa State University and Ames Laboratory. He is an Adjunct Professor at Iowa State University. His research interests are photonics, plasmonics, computational photonics, and electronic properties at surfaces and bulk.
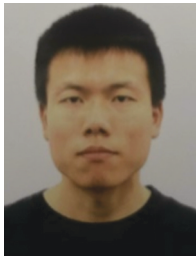
Qiang Li received his B.S. degree in Physics from Fudan University in 2014 and Ph.D. degree in Electrical Engineering from Iowa State University in 2020. He is currently with the University of Michigan at Ann Arbor as a postdoctoral fellow in Electrical Engineering.

Jaeyoun Kim received his Ph.D. degree in Electrical Engineering from the University of Michigan at Ann Arbor in 2003. From 2003–2006, he was with the University of California at Berkeley as a postdoctoral fellow in Berkeley Sensor & Actuator Center (BSAC). In 2006, he joined the Electrical and Computer Engineering Department of Iowa State University where he is currently a Professor.